J. Astrophys. Astr. (2018) 39:70
https://doi.org/10.1007/s12036-018-9561-2

A new technique for understanding magnetosphere–ionosphere coupling using directional derivatives of SuperDARN convection flow

S. N. M. AZIZUL HOQUE[1,*] and FRANCES FENRICH[2]

[1]Department of Physical Sciences, Independent University, Dhaka, Bangladesh.
[2]Department of Physics, University of Alberta, Edmonton, AB T6G 2E9, Canada.
*Corresponding author. E-mail: snmhoque@gmail.com

MS received 6 August 2018; accepted 7 September 2018; published online 23 November 2018

Abstract. The purpose of this paper is to present and evaluate a new technique to better understand ionospheric convection and it's magnetospheric drivers using convection maps derived from the Super Dual Auroral Radar Network (SuperDARN). We postulate that the directional derivative of the SuperDARN ionospheric convection flow can be used as a technique for understanding solar wind–magnetosphere–ionosphere coupling by identifying regions of strong acceleration/deceleration of plasma flow associated with drivers of magnetospheric convection such as magnetic reconnection. Thus, the technique may be used to identify the open–closed magnetic field line boundary (OCB) in certain circumstances. In this study, directional derivatives of the SuperDARN ionospheric convection flow over a four and a half hour interval on Nov. 04, 2001, is presented during which the interplanetary magnetic field was predominantly southward. At each one-minute time point in the interval the positive peak in the directional derivative of flow is identified and evaluated via comparison with known indicators of the OCB including the poleward boundary of ultraviolet emissions from three FUV detectors onboard the IMAGE spacecraft as well as the SuperDARN spectral widths. Good comparison is found between the location of the peak in the directional derivative of SuperDARN flow and the poleward boundary of ultraviolet emissions confirming that acceleration of ionospheric plasma flow is associated with magnetic reconnection and the open–closed boundary.

Keywords. SuperDARN directional derivative technique—ionospheric convection driven by solar wind–magnetosphere–ionosphere coupling—open–closed magnetic field line boundary.

1. Introduction

Coupling between the solar wind and the Earth's magnetosphere occurs predominantly via the process of magnetic reconnection between the solar wind interplanetary magnetic field (IMF) and the terrestrial magnetic field (Dungey 1961). Dayside reconnection results in the transfer of geomagnetic flux from the dayside to the nightside and then back again from nightside to dayside following magnetotail reconnection. This cycle of magnetic merging and flux transfer is the dominant driver of ionospheric convection (Dungey 1961; Siscoe & Huang 1985; Lockwood *et al.* 1990). Other less significant drivers of ionospheric convection include lobe merging and viscous interaction in the low latitude boundary layer (Lu *et al.* 1994; Burch *et al.* 1985). Thus patterns of ionospheric convection are very dependent on IMF direction (Reiff & Burch 1985; Ridley *et al.* 1998; Lockwood & Cowley 1999; Greenwald *et al.* 1990; Ruohoniemi & Greenwald 1996). This dependence is due to differences in the location and type of magnetic merging between the solar wind and magnetospheric field lines (Crooker 1979, 1986; Fenrich *et al.* 2001). A magnetospheric driver will impart its effect upon the ionosphere by accelerating/decelerating the ionospheric plasma flow velocity in the region of the driver. In-situ spacecraft have observed velocity enhancements in outflowing plasma from the region of magnetic reconnection (Sonnerup *et al.* 1981). Basic MHD theory also suggests magnetic curvature forces on newly reconnected field lines should accelerate convective plasma flow out of the reconnection region. Since magnetic reconnection is the dominant driver of convection on both the day and nightside, one would expect significant acceleration/deceleration of the ionospheric convection flow in the vicinity of the footpoints of newly reconnected field lines, i.e. at the open–closed magnetic field line boundary (OCB).

A number of techniques have been developed to identify the OCB. The most reliable of these is the use of particle precipitation boundaries (PPB) measured by low-altitude spacecraft (Evans & Stone 1972; Newell & Meng 1992). However, the OCB measured from PPB is sampled infrequently at a single location rather than estimating boundaries globally and continuously during each overflight (the orbital period is around 100 minutes for DMSP). High-altitude spacecraft auroral imaging overcomes the problem of global and continuous measurement of the OCB by determining high-energy (few keV) electron precipitation (Lockwood *et al.* 1993; Blanchard *et al.* 1995). Assuming a relationship between the poleward border of the auroral oval and the OCB, the poleward edge of auroral luminosity measured by ultraviolet optical imagers (UVI) is used as a proxy for the OCB location (Blanchard *et al.* 1995). The three FUV detectors onboard the IMAGE spacecraft, the Wideband Imaging Camera (WIC) and the Spectrographic imagers SI-12 and SI-13 (Boakes *et al.* 2008; Longden *et al.* 2010) are often used to determine the OCB. In addition, the convection reversal boundary (CRB) can be used as a proxy for the OCB. The CRB and the DMSP OCB are generally in good agreement within crescent-shaped convection cells but is not clearly defined in the midnight region or the larger more circular convection cells (Newell *et al.* 2004). Sotirelis *et al.* (2005) presented statistical evidence that the CRB is on average found $\sim 1^\circ$ equatorward of the DMSP OCB.

The transition from low to high Doppler spectral widths in SuperDARN backscatter has also been tested to find the OCB over large areas of the ionosphere for Earth's dayside (Baker *et al.* 1995) and nightside (Lester *et al.* 2001). Various physical mechanisms have been proposed to explain the change in spectral width across the OCB and these include small scale filamentary field-aligned currents (Schiffler *et al.* 1997), variability of the large-scale convection within the beam-range cell (Villain *et al.* 2002), low-frequency waves (Andre *et al.* 1999), and intense particle precipitation (Ponomarenko & Waters 2003). The latitudes of the SuperDARN spectral width boundary (SWB) and DMSP PPBs have been compared in the night, morning and afternoon sectors (Chisham & Freeman 2004; Chisham *et al.* 2004, 2005a, b; Wild *et al.* 2004). The SWB has been shown to a good proxy for the OCB in the noon and pre-midnight sectors while the SWB is equatorward in the morning and afternoon sectors (Chisham *et al.* 2005a, b).

In this paper we postulate that significant acceleration/deceleration of ionospheric plasma flow occurs in regions where magnetospheric drivers such as magnetic reconnections are active. A new technique is presented which involves the calculation of directional derivatives along streamlines of the ionospheric convection flows derived from the Super Dual Auroral Radar Network (SuperDARN). The technique is applied to a 4 h interval of fairly steady southward IMF and is evaluated by comparing the locations of the positive peak in the directional derivative to proxies of the OCB. Since there are few conjunctions of the SuperDARN data set with the DMSP PPB data during the event and since a significant fraction of the SuperDARN scatter is in the midnight region where it is difficult to identify the CRB, the OCB proxies used for the comparison include only the IMAGE UVI poleward boundaries derived from WIC, SI-12, and SI-13 and the SuperDARN spectral width boundaries. A favorable comparison between the SuperDARN directional derivatives and the OCB proxies will open a discussion of how this new technique provides a new tool to investigate and understand solar wind–magnetosphere–ionosphere coupling.

2. Instrumentation

In this section the details of the instruments and data sets used in this study are discussed.

2.1 *IMAGE FUV observations*

The far ultraviolet (FUV) imager used in NASA's Imager for Magnetopause-to-Aurora Global Exploration (IMAGE) spacecraft observations can be used to find an OCB proxy. The IMAGE spacecraft, in operation from May 2000 to December 2005, was constructed with three detectors on board, with each sensor sensitive to a different wavelength interval and a temporal resolution of 2 minutes (Mende *et al.* 2000a, b). The FUV instrument on the IMAGE spacecraft was constructed with two spectrographic imagers (SI-12 and SI-13) and a wideband imager (WIC). The SI-12 camera is sensitive in the 128 nm band to measure proton precipitation while SI-13 can detect 135.6 nm oxygen emission bands resulting from energetic electron precipitation. The WIC camera can detect the Lyman–Birge–Hopfield (LBH) region of the UV spectrum (140–180 nm). Narrow band UV emissions measured by SI-12 and SI-13 can provide a reasonable OCB proxy in the pre-dawn, dawn and cusp regions (Boakes *et al.* 2008) while wideband auroral UV emission recorded by WIC are an effective OCB proxy in the other MLT sectors (Wild *et al.* 2004). In this paper the IMAGE FUV OCB proxies are obtained from the British Antarctic Survey website (BAS 2013) and are calculated from the double Gaussian function technique developed by Boakes *et al.* (2008) and Longden *et al.* (2010). The original IMAGE data can be accessed from the NASA Space Physics Data Facility (IMAGE 2013).

2.2 *SuperDARN*

The Super Dual Auroral Radar Network (SuperDARN) (Greenwald *et al.* 1995) is an international collaboration operating more than 30 high frequency (HF) radars. These radars monitor ionospheric convection over the northern and southern mid-latitude, high-latitude and polar cap regions. Each radar transmits a short sequence of pulses in the HF band and samples the returned backscatter. The pulse sequence is designed to produce multi lag autocorrelation functions as a function of range. If significant backscatter occurs, the autocorrelation functions (ACF) are fitted to calculate backscattered power, spectral width, and line-of-sight Doppler velocity of plasma flow in the ionosphere. The radar has 16 beams in the most common operating mode. Each beam is approximately 3.2° wide in azimuth. Each radar completes a full scan in either 60 or 120 s (Lester *et al.* 2004). To identify an OCB proxy measured from the SWB, a threshold spectral width value of 200 m/s was used. Chisham *et al.* (2004) show that a threshold of 200 m/s in SWB matches closely with the OCB measured by DMSP, the most reliable proxy of the OCB. The SWB is typically most reliable along the meridionally pointing HF radar beams (Chisham *et al.* 2001). Therefore, the SWB was determined only along the meridional beams of the SuperDARN radars where a clear transition to values greater than the threshold was found.

In this study, two-dimensional convection velocities are required to calculate the directional derivatives of the convection flow speed along streamlines. Thus the SuperDARN convection map potential technique is used to derive the two-dimensional ionospheric convection velocities. Details of this technique and the spherical harmonic fit of the observed Doppler velocity measurements with the statistical model can be found in in Ruohoniemi and Baker (1998), in Ruohoniemi and Greenwald (1996), and references therein. The order of the fit is a variable parameter with higher order fits allowing for smaller scale spatial features. Since this paper is focused on studying the larger-scale dominant drivers of convection, the order of fit is adjusted to 6 which is a lower order of fit than the default of 8. Note that other orders of fit were tested and the results were not significantly affected. Only fitted vectors in the region of backscatter data are deemed reliable and although the directional derivative calculation is done at all points in the convection map, only results in the region of backscatter are used in the analysis.

Figure 1 shows an example of a convection potential map at 8:02 UT, one of our event time points, on November 04, 2001 taken from Virginia Tech website (Superdarn 2014) where the order of fit is 8. The figure shows the convection map velocities only in regions of backscatter color coded to flow speed with contours of constant electrostatic potential (solid and dashed lines). The top-right side of Fig. 1 shows the IMF conditions and the statistical model used.

3. Data analysis

3.1 *Solar wind conditions*

Figure 2 shows the solar wind conditions for the interval 7 UT to 12 UT on November 04, 2001 as provided by the OMNI database. The solar wind conditions were fairly steady during this interval. The interplanetary magnetic field (IMF) B_z component was negative, varying between -5 to 0 nT for most of the period of observation, and went positive for only short periods of time around 8:00 and 10:20 UT. The IMF B_y component remained positive throughout the period of observation with a few short-lived small negative excursions. The dynamic pressure was fairly steady, hovering around 2 nPa for the entire interval. For the SuperDARN convection map fits average values of the IMF given by $B_z = -0.9$ nT, $B_y = 4.4$ nT, and $B_x = 5.3$ nT were used so that any changes in convection between time points were due to the input Doppler velocities and not due to changes in the statistical model.

3.2 *Directional derivative of the convection flow speed technique*

Convection map velocities and electrostatic potential values are output from the generic SuperDARN convection mapping code to a magnetic latitude, magnetic longitude grid fixed with respect to the Earth. To account for the rotation of the grid with the Earth, the convection velocity components at each time point are interpolated

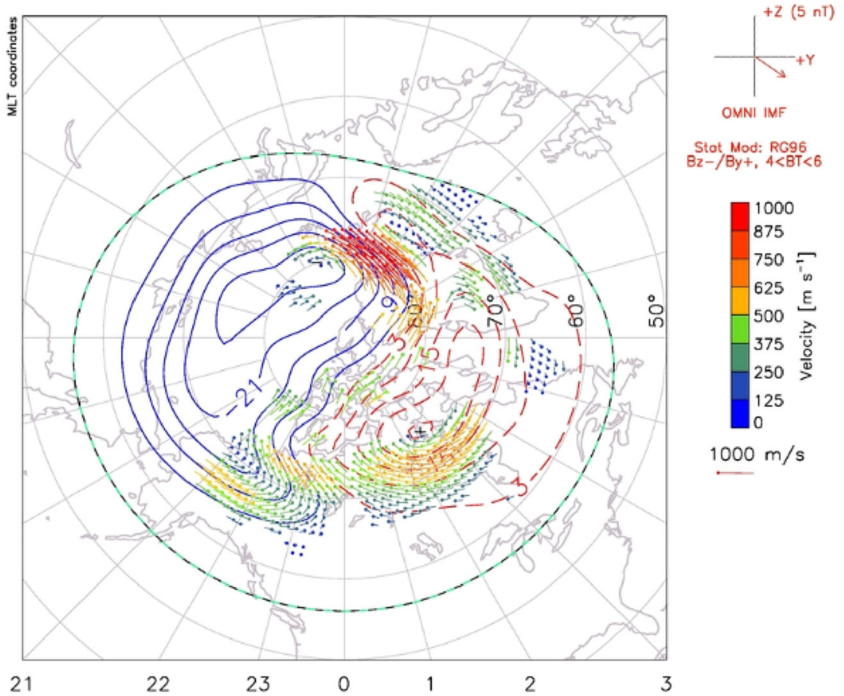

Figure 1. Global convection map estimated from SuperDARN on November 04, 2001, at 08:02 UT. Radial co-ordinates represent magnetic latitudes starting from 50° and the radial lines represent MLT (magnetic local time) meridians, with noon at the top and midnight at the bottom. The dots at the beginning of the vectors indicate the vector locations, the lines show the vector direction, and the colors and length of the lines show the vector magnitude. The velocity scale is shown at the right side of the figure. Solid (dotted) contours are associated with negative (positive) values of electrostatic potential. IMF condition is at the top-right corner of the figure.

to a fixed magnetic latitude, magnetic local time (MLT) grid. The result is a time series of the convection velocity components at each fixed magnetic latitude, magnetic local time grid point. The magnetic latitude/local time grid is a 30 × 180 array with 1° resolution in the latitudinal direction from 60°−90°, and 2° resolution in the longitudinal direction, or .13 h in MLT. The time series at each grid point is then low-pass filtered at 0.5 mHz (equivalent to ∼33 min period) to remove high-frequency variations in the convection map velocities and in particular ultra-low frequency (ULF) field line resonant oscillations which occur at frequencies that range from 0.5 and 5 mHz. To simplify plotting and to make the directional derivative calculation consistent at different latitudes, the grid point locations and the input velocity vectors are converted from the magnetic latitude, magnetic local time coordinate system to an x–y Cartesian coordinate system. In this x–y Cartesian coordinate system, the x-axis corresponds to the 18 and 6 MLT meridians and its scale ranges in value from −30 to 30 units where one unit of distance along the x-axis corresponds to 1° latitude. Likewise, the y-axis corresponds to the 0 and 12 MLT meridians and its scale also ranges from −30 to 30 units with one unit of distance corresponding to 1°. The origin of the x–y coordinate system is the north magnetic pole at 90^0 magnetic latitude. It is a straightforward calculation to convert the grid coordinates and the convection velocities from the input magnetic local time, magnetic latitude coordinate system to this new x–y coordinate system.

At each grid point the streamline gradient in convection flow is subsequently calculated by determining the change in flow speed over a small distance along the streamlines. The directional derivatives values are derived at the same grid points (1° in latitude and 2° in longitude) as the input convection velocities and electric potential values, however, to get a proper measure of the derivative of the flow speed, a smaller distance along the streamlines is required when calculating the change in flow speed. The distance over which the change in flow is calculated is tested at different levels and is adjusted to 0.2 units of distance along the x and y directions, respectively. Other distances were tested and the derivatives were found to be the same for distances smaller than 0.2 units. Note that in order to calculate these derivatives, values of the flow speed were interpolated at the 0.2 unit intervals. A minimum curvature algorithm is applied to interpolate at 0.2 unit

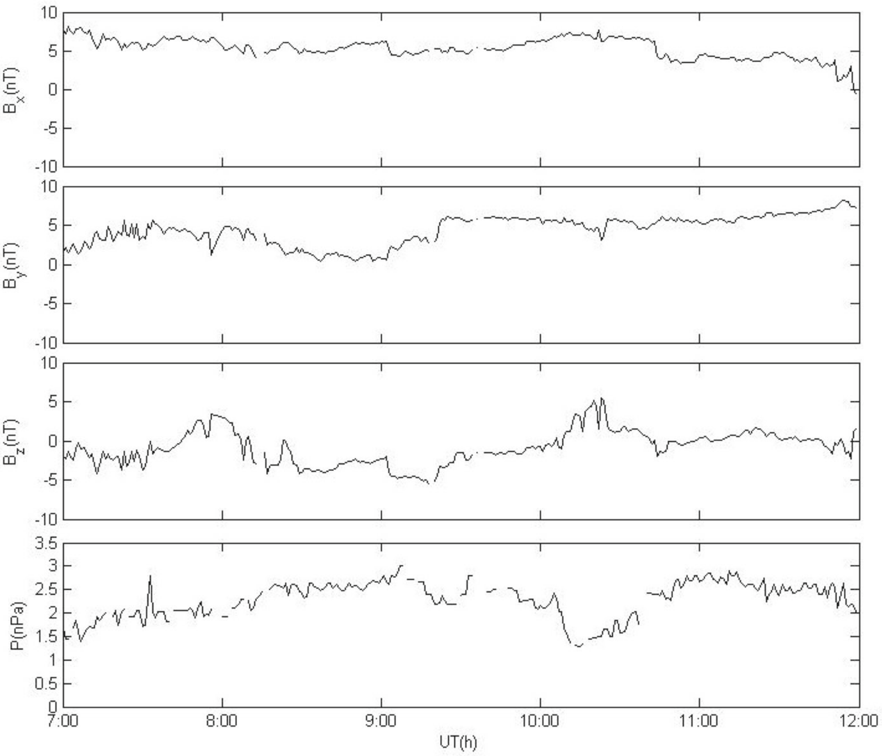

Figure 2. Interplanetary magnetic field (IMF) conditions on November 04, 2001. The top three panels show the GSM components of the IMF and fourth panel represents the solar wind dynamic pressure delayed to the magnetosphere. Data were acquired from the OMNI database and comprise measurements taken from the Geotail spacecraft.

resolution. The directional derivative of flow speed is defined by:

$$\left(\frac{\vec{V}}{|\vec{V}|}\cdot\nabla\right)V \tag{1}$$

where V and $\vec{V}$ are the speed and velocity of plasma flow along the convection streamline, respectively. Since the change in flow is taken over 0.2 unit intervals in the x–y coordinate system, the directional derivative of flow is given in units of m/s per unit distance in the x–y coordinate system.

In the x–y coordinate system Eq. 1 becomes

$$\frac{\left(V_x\hat{\imath} + V_y\hat{\jmath}\right)\cdot\left(\frac{\partial V}{\partial x}\hat{\imath} + \frac{\partial V}{\partial y}\hat{\jmath}\right)}{\sqrt{V_x^2 + V_y^2}} \tag{2}$$

where V_x and V_y are the component of $\vec{V}$ along x and y directions respectively and $\hat{\imath}$ and $\hat{\jmath}$ are the unit vectors along the x and y directions. Note that the magnetic field $\vec{B}$ is approximately perpendicular to the x–y plane (along the z axis).

Figure 3 illustrates via color contours the map of directional derivatives of convection flow speed calculated from the band pass of the original flows of the convection map. The green to red contours correspond to positive values of the convection flow gradient, i.e. increasing flow speed along the streamline, while the blue to black contours correspond to negative values of the convection flow gradient, i.e. decreasing flow speed along the contour. Note that the velocity vectors shown in this plot are the original convection map velocities and not the band-passed velocities from which the directional derivatives are calculated. These velocity vectors and the potential contours are included to indicate the location of backscatter and the shape and location of the convection cells. The positive peak in the directional derivative of flow along a flow streamline, marked as a yellow to red contour (Fig. 3), identifies the region of strongest plasma acceleration and at this time-point is closely associated with the CRB and may be associated with magnetic reconnection between open and closed field lines. Since the convection map velocities are only reliable in regions where ionospheric backscatter exists, the peaks in the directional derivative are considered in the analysis only in the vicinity of regions where ionospheric backscatter exits. Within each 1 h MLT sector the latitudinal location of the peak in the directional derivative is averaged and identified with a plus sign. Note that the higher and lower orders of fit were

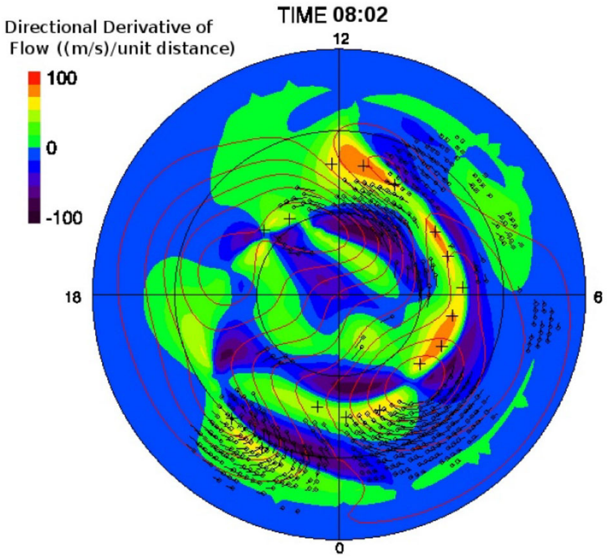

Figure 3. Directional derivative of SuperDARN convection flow map at 08:02 UT in magnetic latitude (MLAT)-magnetic local time coordinates. Solid black circles represent 60°, 70° and 80° MLAT, and radial lines represent MLT meridians at midnight, morning, noon, and evening, with noon at the top and midnight at the bottom. The square dots at the beginning of the vectors indicate the vector locations and the lines show the vector direction and magnitude. The red contours on the left (right) side are associated with negative (positive) values of electrostatic potential. The magnitudes of the potential contours ranges from 3 to 27 kV with 6 kV increment between lines. The plus signs indicate the 'peak' of the directional derivative of plasma flow along the MLT meridian. The directional derivative of the convection flow speed scale is shown at the top-left side of the figure.

tested and key features in the directional derivative of the convection flow speed maps remained consistent. Generally, a single 'peak' or maximum positive value of the SuperDARN convection flow directional derivative along any MLT meridian is observed and identified for analysis. Any other 'peaks' will be secondary peaks. Only the maximum peak is considered in the comparison analysis with the OCB unless there is no data in the vicinity. Secondary peaks may be observed particularly in the midnight region.

4. OCB proxy comparisons

The peak in the directional derivative of SuperDARN convection flow is evaluated via comparison with proxy indicators of the OCB. Figure 4 shows four snapshots in time, at 1 h intervals, of the SuperDARN convection flow directional derivative map including the directional derivative peak locations identified as plus signs. To evaluate if the peak in the directional derivative of flow is associated with magnetic reconnection, the peak locations from SuperDARN are overlaid with the IMAGE FUV OCB proxy locations in Fig. 5. The figures are presented in the same format as that in Fig. 2, with uniform magnetic latitude (starting from 60°) and a magnetic local time coordinate system, with magnetic midnight located at the bottom and noon at the top of each image. The time points are indicated at the top-right of each panel. Note the time-points for SuperDARN and IMAGE are not identical but are as close as possible. In all panels in Fig. 5 the points labeled as red-crosses, blue-pluses, green diamonds, and black-boxes correspond to OCB proxies determined from WIC, SI-12, SI-13, and the peak in the directional derivative of the SupeDARN flow, respectively. Due to data gaps in the SuperDARN backscatter and weak FUV emissions observed by IMAGE it is not possible to identify the directional derivative peak or the OCB proxies at all magnetic local times. This is the reason for data point gaps in Fig. 5. For example, at 07:44:00 UT for SuperDARN (07:43:53 UT for IMAGE spacecraft), the directional derivative peak could not be measured from SuperDARN in the noon to dusk sector, 12.5–19.5 MLT, and early morning sector, 3.5–5.5 MLT, while ultraviolet emissions could not be recorded between 10.5 and 14.5 MLT.

For the Universal time points shown in Fig. 5, the peak in the directional derivative of SuperDARN flow are in fairly good agreement with the OCB measured from the IMAGE FUV detectors in the midnight to dawn to noon magnetic local time sectors. However, in the pre-midnight sector the proxy from the SuperDARN is significantly equatorward of the IMAGE OCB proxies particularly at the earlier Universal time points. For example, at 08:44 UT (top right panel of Fig. 5) the peak in directional derivative of SuperDARN is approximately 8° equatorward of the IMAGE OCB proxies at 21.5, 22.5 and 23.5 MLT. In the corresponding directional derivative of the convection flow speed map, there is a secondary peak in the directional derivative of flow at higher latitudes in the pre-midnight region consistent with the IMAGE OCB proxies. Also note that this secondary peak fall within the dawn convection cell. This suggests that the peak in the directional derivative of SuperDARN flow in the pre-midnight sector is not collocated with the OCB and the magnetic reconnection region.

To provide a more detailed comparison of the SuperDARN flow directional derivative techniqueand the OCB, the temporal evolution of the OCB proxies from

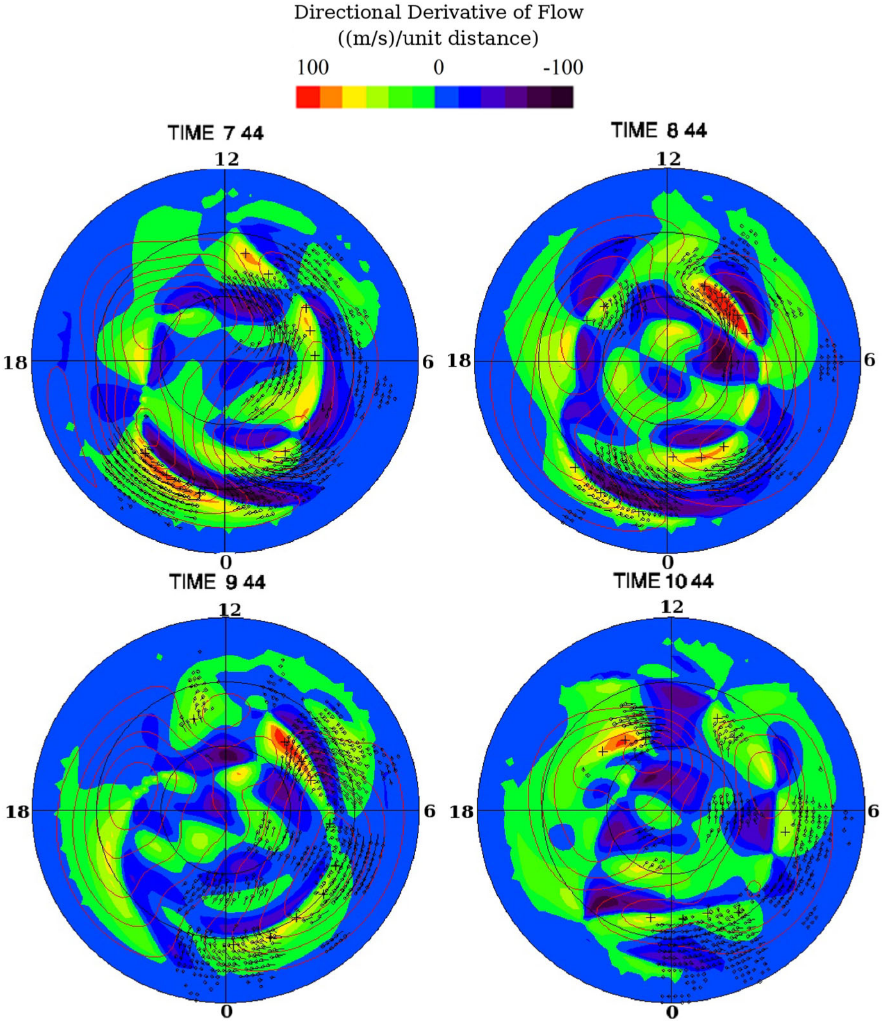

Figure 4. SuperDARN convection flow directional derivatives taken at 1-hour intervals from 07:44–10:44 UT on November 04, 2001 in magnetic latitude (MLAT)-magnetic local time coordinates. The directional derivative of flow is color-coded according to the color scale. Solid black circles represent 60°, 70°, and 80° MLAT, and radial lines represent MLT meridians at midnight, morning, noon, and evening, with noon at the top and midnight at the bottom. The red contours at dusk (dawn) are associated with negative (positive) values of electrostatic potential. The magnitudes of the potential contours start from 3 kV with 6 kV increment between lines. The peak in the directional derivatives of the convection flow are labeled with a plus sign along the magnetic meridian.

the IMAGE FUV poleward boundaires and the Doppler SWB at select magnetic local times are shown in Figs. 6 and 7. Figure 6 shows the temporal evolution of the magnetic latitude of the OCB during the midnight (0.5 MLT), post-midnight (2.5 MLT) and morning (7.5 MLT) sectors, while Fig. 7 corresponds to the afternoon (15.5 MLT), and pre-midnight (21.5 MLT), and midnight (23.5 MLT) sectors. The six different MLTs were chosen based on having the highest amount of data in each quarter of the sector. Although the temporal resolution of the instruments is 2 min, 10 min averages of the OCB locations have been plotted in Figs. 6 and 7. The reason for averaging the OCB locations over 10 min intervals is to make the plots easier to view by reducing the number of plotted points and to provide an estimate of the measurement error in the OCB locations by taking the standard deviation over the 10 minute intervals. The standard deviations were typically 0.35°, 0.62°, 0.73°, 0.68°, 0.49° for the SuperDARN flow directional derivatives, WIC, SI-12, SI-13, and SuperDARN SWB OCB proxies, respectively. Since only meridional beams are used to determine Doppler SWBs, the data coverage may not be the same as data obtained with the SuperDARN convection flow directional derivative technique. For example, the Doppler SWB could not be determined at 15.5 MLT and 21.5 MLT (Fig. 7) and few data were present for other local times.

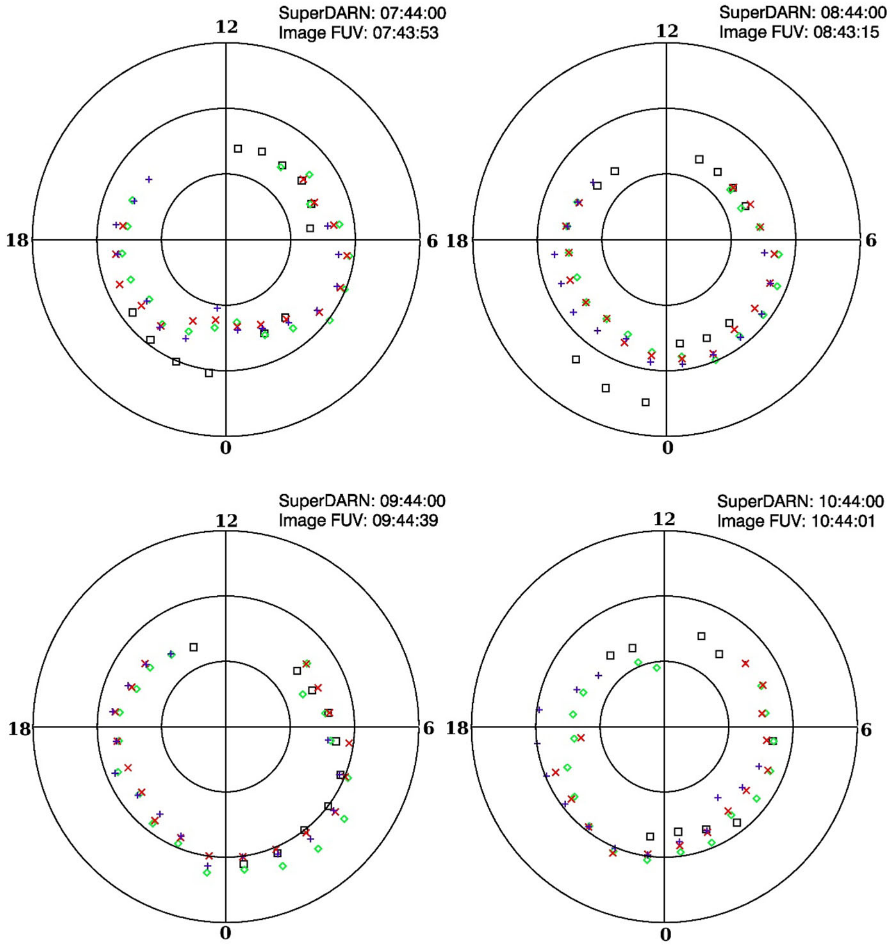

Figure 5. The peak location of the SuperDARN convection flow directional derivative (black-box), and the OCB proxy from IMAGE WIC (red-cross), SI-13 (green-diamond), and SI-12 (blue-plus) taken at 1-hour intervals from 07:44–10:44 UT on November 04, 2001. All panels are presented in MLAT-magnetic local time coordinates. Solid black circles represent 60°, 70°, and 80° MLAT, and radial lines represent MLT meridians at midnight, morning, noon, and evening, with noon at the top and midnight at the bottom. The top-right corner of each panel indicates the time at which the OCB was measured from the poleward boundary of the UV emission of the IMAGE FUV detectors and SuperDARN.

To investigate the similarity of the latitudinal variations with time of the different techniques, the correlation coefficients between the peak in directional derivative of SuperDARN flow technique and each of the IMAGE FUV OCB proxies are calculated at each MLT and are shown in Fig. 8(a). The correlations are high, above values of 0.5, at all MLTs with data coverage except at 4.5 and 5.5 MLT where coefficient values are 0.4 and 0.3, respectively. Correlation coefficients are missing from 8.5 MLT to the pre-midnight sector due to insufficient data for statistical analysis. The highest correlations of 0.75 are found with the WIC data, typically corresponding to the Lyman–Birge–Hopfield (LBH) region of the UV spectrum ($\sim$140$-$180 nm).

To provide a measure of the absolute agreement between the different techniques, the square root of the mean of the squares of the deviations between the peak of SuperDARN flow directional derivative locations and the three IMAGE OCB proxies are calculated at each MLT. The lower panel of Fig. 8 shows these root mean square deviations which were calculated using the 10 minute data point averages as shown in Figs. 6 and 7. SuperDARN-WIC pair data are marked ‘WIC’ (red-circle), SuperDARN-SI-12 pair data are marked ‘SI-12’ (blue-plus), and SuperDARN-SI-13 pair data are marked ‘SI-13’ (green-star). The root mean square deviations range from 0.8° to 3° magnetic latitude with the WIC instrument typically having the lowest root mean square deviation with SuperDARN. Relatively higher root mean square deviation values are observed in the pre-midnight sector, a trend that was also evident in Fig. 5 (07:44 UT and 08:44 UT), and Fig. 7 (at 21.5

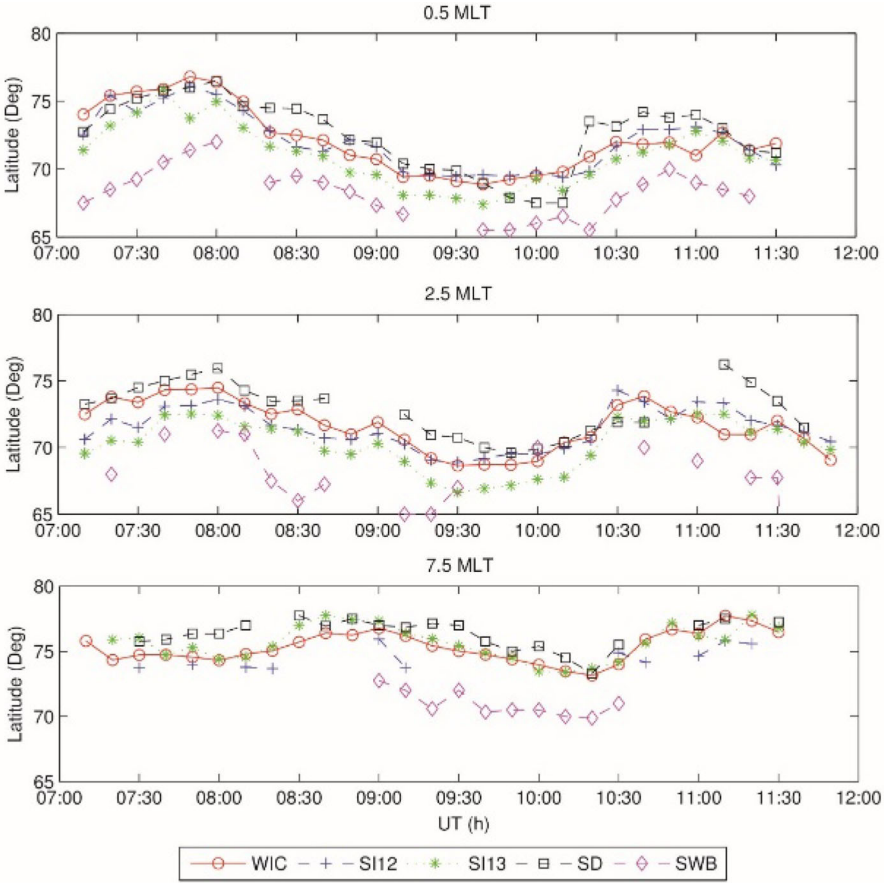

Figure 6. Temporal evolution (with 10 minute intervals) of latitudinal locations of the OCB measured from the three IMAGE FUV detectors, the SuperDARN flow directional derivatives, and the SWB. The upper, middle, and lower panels show OCB locations at 0.5 MLT, 2.5 MLT, and 7.5 MLT sectors respectively. In each case, OCBs measured from three ultraviolet cameras are labeled 'red-circle' (corresponding to WIC), 'blue-plus' (corresponding to SI-12), and 'green-star' (corresponding to SI-13). The directional derivative of SuperDARN flow measurements and Doppler SWBs are superimposed as 'black-box' and 'magenta-diamond' shapes.

MLT). The lowest root mean square deviation occurred in the morning (6.5 and 7.5 MLT). This is also evident in Fig. 6, where the SuperDARN OCB was co-located close to the OCB at 7.5 MLT detected from the WIC imager during the entire interval.

5. Discussion

Figures 6, 7 and 8 demonstrate the correspondence between the peak in the directional derivative of SuperDARN flow and the OCB proxies for the 4.5 h interval on November 1, 2004 during which IMF B_z is predominantly negative, and IMF B_y positive. In particular, in the midnight to post-midnight region, see the 23.5, 0.5 and 2.5 MLT panels of Figs. 6 and 7, both the directional derivative peak and the OCB proxies show the same latitudinal variation with time. At the beginning of the interval all measured parameters move poleward and reach their most poleward extent around 75° latitude at $\sim 8:00$ UT. They then move $\sim 8°$ equatorward over a 2 h interval and then return poleward from 10:15 UT to 11:00 UT to reach latitudes around 75°, after which they begin to move equatorward again.

This repeated contraction/expansion of the polar cap over the interval of interest is consistent with the changes in the IMF B_z component as seen in Fig. 1. The equatorward movements of the peak in the directional derivative of flow and the OCB proxies correspond to the periods of negative IMF B_z and the poleward motions to the positive transitions of IMF B_z. The high correlation coefficients above 0.5 between the directional derivative peak locations and the IMAGE OCB proxies in the midnight to post-midnight MLT sectors together with the 1.5–2.5° latitude root-mean-square differences between them confirms that the peak in the

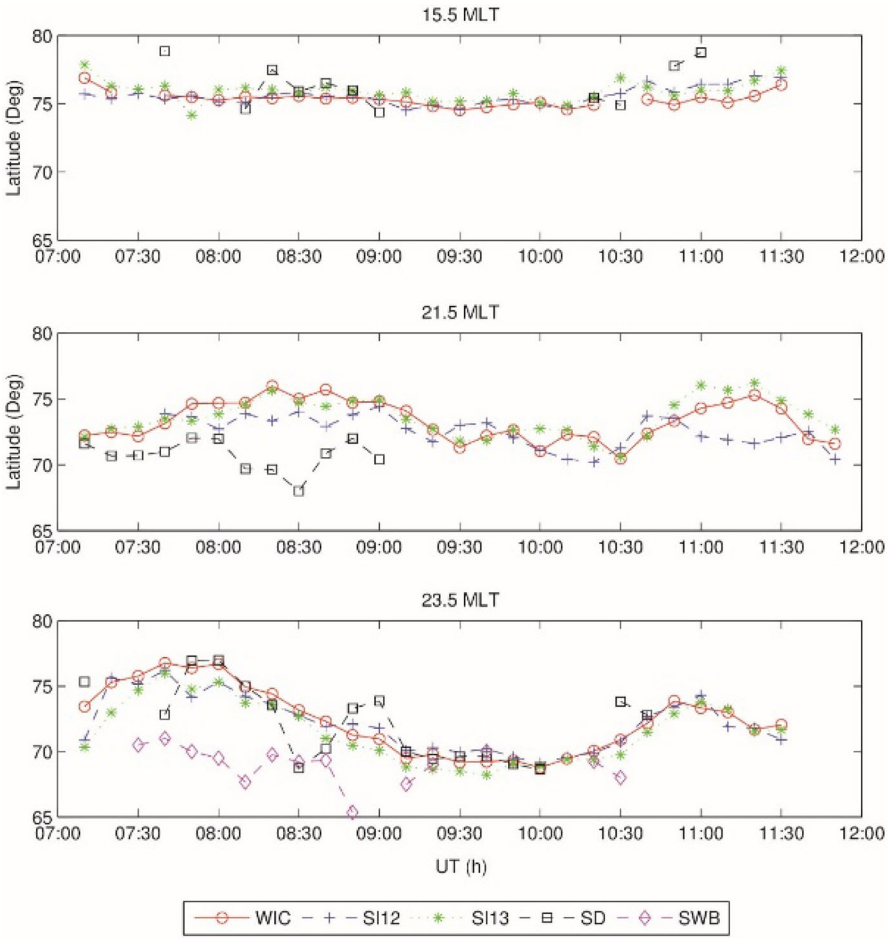

Figure 7. Temporal evolution (with 10 minute intervals) of the latitudinal location of the OCB measured from the three IMAGE FUV detectors, the SuperDARN convection flow directional derivatives, and the SWB. The upper panel shows the afternoon (15.5 MLT) sector, the middle panel shows the pre-midnight (21.5 MLT), and the lower panel shows the midnight (23.5 MLT) sector OCB locations during the specific period of time. The figure is presented in the same format as that in Fig. 6.

directional derivative of flow closely tracks the OCB in the midnight-post-midnight sector during southward IMF conditions. This result suggests that within the nightside portion of the dawn convection cell the deceleration/acceleration of plasma convection flow is associated with magnetic reconnection in the magnetotail and the positive peak in the directional derivative of flow can be a good indicator of the location of the OCB and the footpoints of recently reconnected field lines.

In the pre-midnight sector there are significant differences between the latitudinal location of the IMAGE OCB proxies and the peak in the SuperDARN directional derivative of flow, see the 07:44 UT and 08:44 UT time points in Fig. 5 and the 21.5 MLT panel in Fig. 7. The pre-midnight region is a complex region encompassing the Harang discontinuity. During IMF B_z negative and IMF B_y positive conditions there is a significant overlap of the dusk and dawn convection cells in this region. This results in multiple peaks in the directional derivative of flow along a given MLT meridian with the equatorward peak being the most dominant. However, the secondary peak at higher latitude is consistent with the IMAGE OCB proxy locations (see the first 07:44 and 08:44 panels of Figs 4 and 5) and is an extension of the dominant peak in the directional derivative within the dawn convection cell. This suggests that in the pre-midnight region the secondary peak of the directional derivative may be associated with the OCB and magnetic reconnection while the strong deceleration and subsequent acceleration of the plasma flow further equatorward along the convection streamlines lies within the convection reversal region of the dusk cell. Thus, in the pre-midnight region, the largest peak in the directional derivative of flow is not directly associated with magnetic reconnection but rather some other type of convective driver in the magnetotail. In the

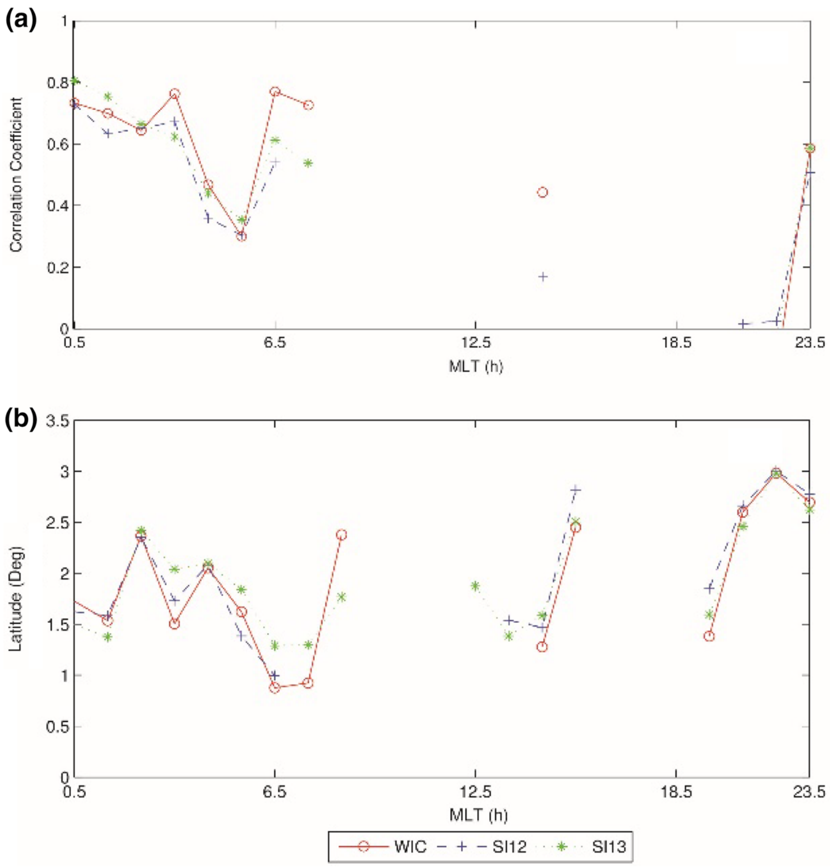

Figure 8. Correlation coefficients (panel a) and root mean square deviation (panel b) between SuperDARN and the three IMAGE FUV detectors at each MLT. In each case, the points labeled 'red-circle,' 'blue-plus,' and 'green-star' correspond to WIC-SuperDARN, SI-12-SuperDARN, and SI-13-SuperDARN correlations. In the lower panel, the root mean square deviations are measured in magnetic latitude.

pre-midnight region, the convective driver is associated with the convection reversal and plasma acceleration on closed field lines ~5 − 7° equatorward of the IMAGE FUV OCB (Newell *et al.* 2004).

In the dusk and dawn sectors both the peak in directional derivative and the IMAGE OCB proxies (see the lower panel of Fig. 6 and upper panel of Fig. 7) are less responsive to the IMF conditions and remain fairly steady around 75° magnetic latitude throughout the interval. There is high correlation (0.5–0.8) and small deviation (~1° latitude) between the directional derivative peak and the OCB near dawn and a 1.5° to 2.5° deviation at dusk (see Fig. 8). The dusk and dawn OCB regions are generally located near the center of the convection cells which tend to be associated with viscous interaction in the low latitude boundary layer. Thus the directional derivatives in this region may be due to this viscous interaction process.

Figures 6 and 7 indicate that the Doppler SWB is not a reliable OCB proxy in the midnight to dawn sectors and therefore is not useful in the evaluation of the directional derivative technique. The SWB is consistently found to be located at much lower latitudes than the IMAGE FUV OCB proxies as was found in previous studies (Chisham *et al.* 2005a, b). The average latitudinal difference between the Doppler SWB and the IMAGE OCB proxy measurements was 4° equatorward with a maximum of 7° at midnight.

6. Conclusions

This paper presents a new technique using SuperDARN directional derivatives of convection flow. A case study comparison of the peak in the directional derivative of SuperDARN flow and IMAGE FUV OCB proxy techniques is made at a variety of magnetic local times during an interval of negative IMF B_z and positive IMF B_y. High correlation is found between the positive maxima in the directional derivative of SuperDARN flow and the open–closed field line boundary at local times in the midnight to dawn sectors and the dusk sector.

These results support the hypothesis that significant acceleration/deceleration of ionospheric plasma flow occurs in regions where magnetospheric drivers such as magnetic reconnection and viscous interactions are active. However, due to overlap of the dusk and dawn convection cells in the pre-midnight sector during IMF B_z negative and IMF B_y positive conditions the association between the SuperDARN directional derivatives, the OCB, and magnetic reconnection is unclear. In this paper our study is limited to the case when IMF B_z is negative and B_y is positive. The asymmetry of the dusk and dawn cells occurs primarily at midnight and post-midnight along the MLT depending on the sign of IMF By. If IMF B_z and B_y are negative, shapes of the dusk and dawn cell are crescent and rounded respectively. The relation between the large scale ionospheric convection and IMF conditions has been understood for a number of years (Heppner & Maynard 1987; Ruohoniemi & Greenwald 1995). Overlap between the two cells and deviation between the IMAGE FUV OCB and the SuperDARN directional derivatives is expected to occur in the pre-midnight sector for the IMF B_z and B_y negative case as well.

Although further analysis of this technique during different solar wind conditions is required, this study clearly shows that this new SuperDARN directional derivative of flow technique has the potential to improve our understanding of the magnetopheric drivers of ionospheric convection and may be used as a proxy for the OCB and the footpoints of magnetic reconnection in the magnetotail. An improved understanding of the magnetospheric drivers of ionospheric convection will lead to a more complete characterization of the state of coupling between the solar wind, magnetosphere and ionosphere and to advancement in space weather forecasting/nowcasting.

Acknowledgements

This work was supported by the Natural Sciences and Engineering Research Council of Canada. The authors thank the SuperDARN PIs for providing the SuperDARN data and software. We gratefully acknowledge the IMAGE FUV Imager team and PI Stephen Mende. Auroral boundary data were derived and provided by the British Antarctic Survey based on IMAGE satellite data. The SuperDARN data were collected from superdarn.org. The OMNI data were obtained from the GSFC/SPDF OMNIWeb interface.

References

Andre R., Pinnock M., Rodger A. S. 1999, Geophys. Res. Lett. 26, 3353–3356

Baker K. B., Dudeney J. R., Greenwald R. A., Pinnock M., Newell P. T., Rodger A. S., Mattin N., Meng C.-I. 1995, J. Geophys. Res. 100, 7671–7695

BAS 2013, https://legacy.bas.ac.uk/bas_research/our_research/az/magnetic_reconnection/auroral_boundary_location_method.html

Blanchard G. T., Lyons L. R., Samson J. C., Rich F. J. 1995, J. Geophys. Res. 100, 7855–7862

Boakes P. D., Milan S. E., Abel G. A., Freeman M. P., Chisham G., Hubert B., Sotirelis T. 2008, Annales Geophysicae 26, 2759–2769

Burch J. L., Reiff P. H., Menietti J. D., Heelis R. A., Hanson W. B., Shawhan S. D., Shelley E. G., Sugiura M., Wiemer D. R., Winningham J. D. 1985, J. Geophys. Res. 90, 1577–1593

Chisham, G., Pinnock, M., Rodger, A. S. 2001, J. Geophys. Res. 106, 191–202

Chisham G., Freeman M. P. 2004, Ann. Geophys. 22, 1187–1202

Chisham G., Freeman M. P., Sotirelis T. 2004, Geophys. Res. Lett. 31, L02804

Chisham G., Freeman M. P., Lam M. M., Abel G. A., Sotirelis T., Greenwald R. A., Lester M. 2005a, Ann. Geophys. 12, 3645–3654

Chisham G., Freeman M. P., Sotirelis T., Greenwald R. A., Lester M., Villain J.-P. 2005b, Ann. Geophys. 23, 733–743

Chisham G., Lester M., Milan S. E., Freeman M. P., Bristow W. A., Grocott A., McWilliams K. A., Ruohoniemi J. M., Yeoman T. K., Dyson P. L., Greenwald R. A., Kikuchi T., Pinnock M., Rash J. P. S., Sato N., Sofko G. J., Villain J.-P., Walker A. D. M. 2007, Surveys in Geophysics 28, 33–109

Crooker N. U., 1986, Geophys. Res. Lett. 13, 1063–1066

Crooker N. U. 1979, J. Geophys. Res. 84, 951–959

Dungey, J. W. 1961, Phys. Rev. Lett. 6, 47–48

Evans L. C., Stone, E. C. 1972, J. Geophys. Res. 77, 5580–5584

Fenrich F. R., Luhmann J. G., Fedder, J. A., Slinker S. P., Russell C. T. 2001, J. Geophys. Res. 106, 18789–18802

Greenwald R. A., Baker K. B., Ruohoniemi J. M., Dudeney J. R., Pinnock M., Mattin N., Leonard J. M., Lepping R. P. 1990, J. Geophys. Res. 95, 8057–8072

Greenwald R. A., Baker K. B., Dudeney J. R., Pinnock M., Jones T. B., Thomas E. C., Villain J.-P., Cerisier J.-C., Senior C., Hanuise C., Hunsucker R. D., Sofko G., Koehler J., Nielsen E., Pellinen R., Walker A. D. M., Sato N., Yamagishi, H. 1995, Space Sci. Rev. 71, 761–796

Heppner J. P., Maynard N. C. 1987, J. Geophys. Res. 92:4467–4489

IMAGE 2013, https://spdf.sci.gsfc.nasa.gov/pub/data/image/fuv

Lester M., Milan S. E., Besser V., Smith, R. 2001, Ann. Geophys. 19, 327–339

Lester, M., Chapman, P. J., Cowley, S. W. H., Crooks, S. J., Davies, J. A., Hamadyk, P., McWilliams, K. A., Milan, S. E., Parsons, M. J., Payne, D. B., Thomas, E. C., Thornhill, J. D., Wade, N. M., Yeoman, T. K., Barnes, R. J. 2004, Ann. Geophys. 22, 459–473. https://doi.org/10.5194/angeo-22-459-2004

Lockwood M., Cowley S. W. H., Freeman M. P. 1990, J. Geophys. Res. 95, 7961–7972

Lockwood M., Cowley S. W. H. 1999, J. Geophys. Res. 104, 4387–4391

Lockwood M., Carlson Jr. H. C., Sandholt P. E. 1993, J. Geophys. Res. 98, 15,571–15,587

Longden N., Chisham G., Freeman M. P., Abel G. A., Sotirelis T. 2010, Ann. Geophys. 28, 1659–1678

Lu G., Richmond A. D., Emery B. A., Reiff P. H, de la Beaujardiere O., Rich F. J., Denig W. F., Kroehl H. W., Lyons L. R., Ruohoniemi J. M., Friis-Christensen E., Opgenoorth H., Persson M. A. L., Lepping R. P., Rodger A. S., Hughes T., McEwin A, Dennis S., Morris R., Burns G., Tomlinson L. 1994, J. Geophys. Res. 99, 6491–6510

Mende S. B., Heetderks H., Frey H. U., Lampton M., Geller S. P., Habraken S., Renotte E., Jamar C., Rochus P., Spann J., Fuselier S. A., Gerard J.-C., Gladstone R., Murphree S., Cogger L. 2000a, Space Sci. Rev. 91, 243–270

Mende S. B., Heetderks H., Frey H. U., Stock J. M., Lampton M., Geller S. P., Abiad R., Siegmund O. H. W., Habraken S., Renotte E., Jamar C., Rochus P., Gerard J.-C., Sigler R., Lauche H. 2000b, Space Sci. Rev. 91, 287–318

Newell P. T., Meng, C. I. 1992, Geophys. Res. Lett. 19, 609–612

Newell P. T., Ruohoniemi J. M., Meng C.-I. 2004, J. Geophys. Res. 109, A10206

Ponomarenko P. V., Waters C. L. 2003, Geophys. Res. Lett. 30:1122

Reiff P. H., Burch J. L. 1985, J. Geophys. Res. 90, 1595–1609

Ridley A. J, Lu G., Clauer C. R., Papitashvili V. O. 1998, J. Geophys. Res. 103, 4023–4039

Ruohoniemi J. M., Greenwald R. A. 1995, Geophys. Res. Lett., 22, 1121–1124

Ruohoniemi J. M., Greenwald R. A. 1996, J. Geophys. Res. 101, 21,743–21,763

Ruohoniemi J. M., Baker, K. B. 1998, J. Geophys. Res. 103, 20,797–20,811

Schiffler A., Sofko G., Newell P. T., Greenwald R. A. 1997, Geophys. Res. Lett. 24, 3149–3152

Simon S. G., Rhuohoniemi, J. M. 2000, J. Geophys. Res. 105, 23,005–23,014

Siscoe G. L. and Huang T. S. 1985, J. Geophys. Res. 90, 543–547

Sonnerup, B. U. O., Paschmann, G., Papamastorakis, I., Sckopke, N., Haerendel, G., Bame, S. J., Asbridge, J. R., Gosling, J. T., Russell, C. T. 1981, J. Geophys. Res., 86, 10,049–10,067

Sotirelis T., Ruohoniemi J. M., Barnes R. J., Newell P. T., Greenwald R. A., Skura J. P., Meng C.-I. 2005, J. Geophys. Res. 110, A06302

Superdarn 2014. http://superdarn.org

Villain, J-P., Andre R., Pinnock M., Greenwald, R. A., Hanuise, C. 2002, Ann. Geophys. 20, 1769–1781

Wild J. A., Milan S. E., Owen C. J., Bosqued J. M., Lester M., Wright D. M., Frey H., Carlson C. W., Fazakerley A. N., Rème H. 2004, Ann. Geophys. 22, 3625–3639